

Observation of spin-structure of ultralong-range Rydberg molecules

Markus Deiß,¹ Shinsuke Haze,¹ Joschka Wolf,¹ Limei Wang,¹ Florian Meinert,² Christian Fey,³ Frederic Hummel,³ Peter Schmelcher,^{3,4} and Johannes Hecker Denschlag¹

¹*Institut für Quantenmaterie and Center for Integrated Quantum Science and Technology IQST, Universität Ulm, 89069 Ulm, Germany*

²*5. Physikalisches Institut and Center for Integrated Quantum Science and Technology IQST, Universität Stuttgart, 70569 Stuttgart, Germany*

³*Zentrum für optische Quantentechnologien, Universität Hamburg, Fachbereich Physik, 22761 Hamburg, Germany*

⁴*The Hamburg Centre for Ultrafast Imaging, Universität Hamburg, 22761 Hamburg, Germany*

(Dated: April 18, 2022)

We present an experimental and theoretical study of the spin- and vibrational states of $16P - 5S$ ultralong-range Rb_2 Rydberg molecules that are bound in the second outermost potential well. Due to resonant p -wave interaction, the admixture of a butterfly state, and the combination of spin-spin and spin-orbit couplings these molecules feature non-trivial spin state energy level manifolds. By carrying out Rydberg spectroscopy we observe several vibrational ladders. Each ladder exhibits a characteristic multiplet substructure which facilitates assigning a spin state to each level. Our calculations show that a specific type of spin-orbit interaction can significantly contribute to the multiplet line splittings. This spin-orbit interaction is given by the coupling between the total electron spin and the orbital angular momentum of the Rydberg electron in the reference frame of the ground state atom. Furthermore, we find that the diabaticity of the molecular motion across an avoided crossing in the potential energy curve has a strong impact on the vibrational level structure. Our investigation paves the way for further in-depth studies of subtle interaction mechanisms in Rydberg molecules.

I. INTRODUCTION

Since their prediction almost twenty years ago [1] and boosted by their first observation [2], ultralong-range Rydberg molecules have become a research area of major interest (for a review, see, e.g. [3]). In such exotic molecules the scattering of the Rydberg electron off the ground state atom leads to molecular bound states. So far, a number of experimental studies have been carried out on different atomic species (Rb, Cs, Sr), investigating molecules correlated with S , P , or D Rydberg atomic states (e.g. [2, 4–14]). These studies comprise also trilobite dimers [1, 6, 14], which can feature huge permanent electric dipole moments [6], and butterfly dimers [15, 16] that were observed recently [7]. While the binding mechanism for trilobite molecules relies on s -wave scattering, p -wave scattering has to be included in order to theoretically describe butterfly molecules. Typically, molecules are bound in the wells of the oscillatory potential energy curves connected to the Rydberg electron wave function. However, bound states can also be obtained by internal quantum reflection at a steep potential drop caused by a resonant p -wave interaction [17], i.e. even in the absence of a regular inner potential well.

Besides the electronic orbital degrees of freedom, Rydberg molecules also exhibit interesting dynamics due to their spin degrees of freedom. In the presence of spin-dependent scattering channels, hyperfine coupling effectively mixes the collective electronic singlet and triplet state of the valence electrons [8, 9, 12, 18–20]. Furthermore, a spin-orbit coupling connected to the relative orbital angular momentum between the Rydberg electron and the ground state atom has been predicted [21–23] which, e.g., leads to a modification of the butterfly curves and dipole moments of the corresponding molecular states, especially when the kinetic energy of the Rydberg electron is close to the p -wave shape resonance. Although some preliminary indication of this spin-orbit interaction has been found recently [21, 24] no clear experimental evidence

has been demonstrated so far.

In the present work we investigate the properties of ultralong-range $^{87}\text{Rb}_2$ Rydberg molecules consisting of a $5S_{1/2}$ ground state atom and a $16P_{3/2}$ Rydberg atom. The molecular bound states are located in the second outermost well of the Born-Oppenheimer potential energy curve. That specific well is strongly distorted by the p -wave shape resonance. This, together with spin-spin and spin-orbit interactions gives rise to a characteristic level structure which we explore both experimentally and theoretically. The experiments are carried out using photoassociation spectroscopy for an ultracold cloud of spin-polarized ground state ^{87}Rb atoms. Rydberg molecules, produced via photoassociation, are detected in an ion trap after ionization. We observe several vibrational ladders, each belonging to a different spin state. These spin states can be distinguished in our spectra since characteristic single, double, and triple line multiplet substructures of respective vibrational levels are found. We present theoretical calculations based on a pseudopotential Hamiltonian [21] which agree very well with the experimental measurements on a qualitative level and reasonably well on a quantitative level in view of the complexity of the potential structure to be modeled here.

This article is structured as follows. In section II we provide a simplistic description of the investigated Rydberg molecules and the corresponding potential energy curves in order to establish a basis for the following discussion. Subsequently, in section III we introduce our experimental scheme and describe the obtained spectroscopic data in detail. Section IV is devoted to an introduction of different types of spin-spin and spin-orbit coupling mechanisms which are included in our theoretical model. This model will be used to interpret our experimental data in section V in terms of comparing the results of theoretical simulations assuming adiabaticity or diabaticity.

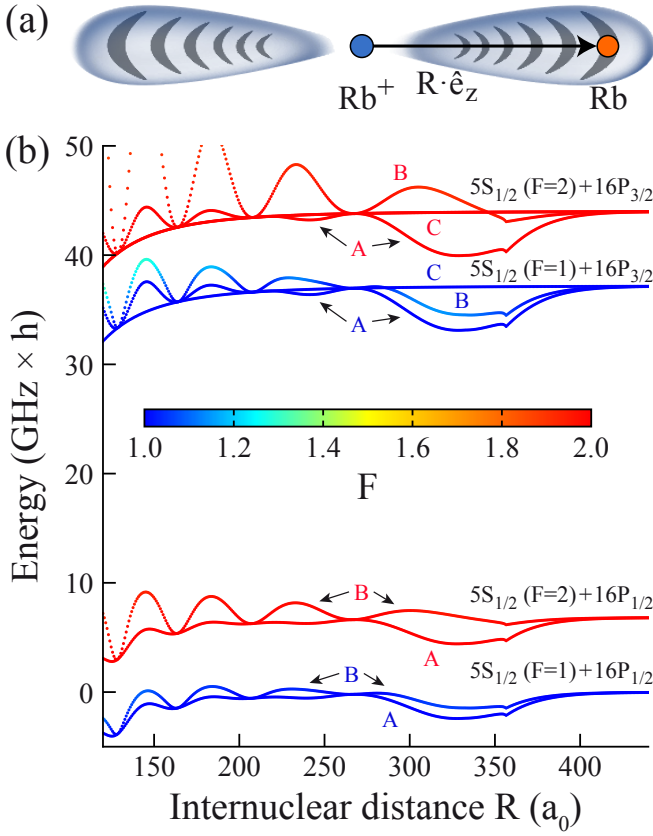


FIG. 1. (a) Sketch of an ultralong-range Rydberg molecule, consisting of a Rb^+ ionic core, an electronic Rydberg P -state orbital, and a ground state Rb atom which is located at position $\vec{R} = R\hat{e}_z$ relative to the ionic core. (b) The molecular Born-Oppenheimer potentials of the above setup when s -wave interactions between electron and ground state atom are taken into account but p -wave interactions are neglected. From each atomic asymptote two oscillatory potentials emerge. They have $|m_j| = 1/2$ and feature the nodes of the electronic wave function. The deeper PECs (marked with A) are associated with pure triplet scattering and the shallower PECs (marked with B) are associated with mixed singlet/triplet scattering. The PECs labeled with C have $|m_j| > 1/2$ and do not show an oscillatory behavior.

II. ULTRALONG-RANGE RYDBERG MOLECULE

Figure 1(a) shows a simplified sketch of the ultralong-range Rydberg molecule. The electronic $16P$ -orbital of the Rydberg atom overlaps with the ground state atom at distance R . The atom and the electron can locally interact, which leads to molecular binding. To a first approximation the interaction between atom and electron can be modeled by a short-range, s -wave Fermi-type pseudopotential. Figure 1(b) shows the corresponding Born-Oppenheimer potential energy curves (PECs). The oscillatory behavior of the PECs reflects the radial wave function of the Rydberg electron. In the potential wells of the PECs vibrational bound states of ultralong-range Rydberg molecules exist. For large separations, $R \gtrsim 400 a_0$, the PECs go over into the atomic asymptotes corresponding to the Rydberg levels ($16P_{1/2}$ and $16P_{3/2}$) and the hyperfine

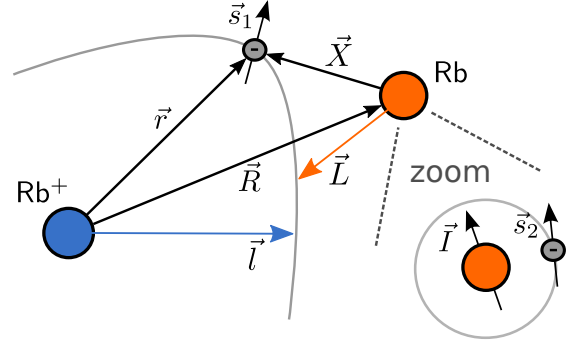


FIG. 2. Composition of the molecular system: A ground state atom is located at position \vec{R} relative to the ionic core of a Rydberg atom. The Rydberg electron with spin \vec{s}_1 is located at position \vec{r} with orbital angular momentum \vec{l} relative to the ionic core and at position \vec{X} with orbital angular momentum \vec{L} relative to the ground state atom. Furthermore, the ground state atom possesses an electronic spin \vec{s}_2 and a nuclear spin \vec{I} .

states ($F = 1$ and $F = 2$) of the ground state atom. Here, a_0 is the Bohr radius. The colors of the curves indicate the expectation value of the F -quantum number of the ground state atom. At shorter distances hyperfine states can get mixed.

The PECs are calculated using the electronic Hamiltonian

$$H = H_{\text{Ryd}} + H_{\text{g}} + V. \quad (1)$$

H_{Ryd} describes the interaction of the Rydberg electron in the potential of the ionic Rb^+ core. The electron has spin \vec{s}_1 and angular momentum \vec{l} (see Fig. 2). H_{Ryd} has eigenstates $\phi_{nljm_j}(\vec{r})$ with energies E_{nlj} , where n is the principle quantum number and $\vec{j} = \vec{l} + \vec{s}_1$ is the total angular momentum of the Rydberg electron. The energies E_{nlj} are taken from spectroscopic measurements [25–27] and are used as input to analytically determine the long-range behavior (larger than several a_0) of $\phi_{nljm_j}(\vec{r})$ in terms of appropriately phase shifted Coulomb wave functions. Knowledge on the wave functions for smaller radii is not necessary for our purpose. $H_{\text{g}} = A\vec{I} \cdot \vec{s}_2$ represents the Hamiltonian of hyperfine interaction in the ground state atom with the electronic spin \vec{s}_2 , the nuclear spin \vec{I} , and $A = 3.417 \text{ GHz} \times h/\hbar^2$ [28]. H_{g} has eigenstates $|Fm_F\rangle$, where $\vec{F} = \vec{I} + \vec{s}_2$. The term V describes the interaction between the Rydberg electron and the ground state atom which is largely determined by the orbital angular momentum \vec{L} of the Rydberg electron in the reference frame of the ground state atom. For $L = 0$ there is s -wave interaction, while p -wave interaction is given for $L = 1$. We employ a generalized Fermi pseudopotential [21, 29]

$$V = \sum_{\beta} \frac{(2L+1)^2}{2} a(L, S, J, k) \frac{\delta(X)}{X^{2(L+1)}} |\beta\rangle \langle \beta| \quad (2)$$

(using atomic units), where $X = |\vec{r} - \vec{R}|$ is the absolute distance between the Rydberg electron and the ground state atom (see Fig. 2) and β is a multi-index that defines projectors onto the different scattering channels $|\beta\rangle = |LSJM_J\rangle$.

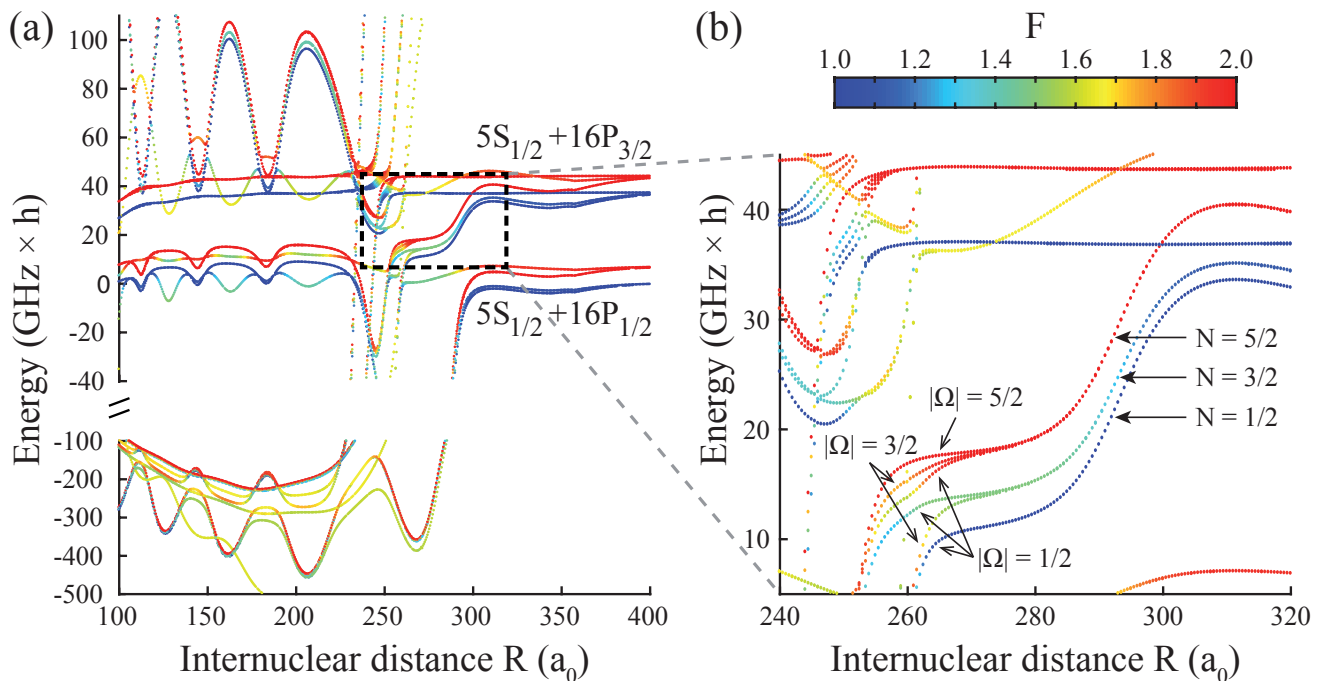


FIG. 3. (a) The molecular PECs correlated to the $5S_{1/2} + 16P_j$ atomic asymptotes for $j \in \{1/2, 3/2\}$ and different hyperfine states $F \in \{1, 2\}$ of the $5S_{1/2}$ atom. The color code represents the expectation value of the quantum number F . In contrast to Fig. 1(b), p -wave interactions are included here. Due to resonant p -wave interactions at internuclear separations $R \approx 250 a_0$ steep butterfly PECs form that cut through the P -state PECs, creating several avoided crossings. At shorter distances the butterfly PECs bend over, forming potential wells in the energy range of about -500 to $-100 \text{ GHz} \times h$. (b) Zoom into the dashed rectangle in (a). At energies between about 10 to $20 \text{ GHz} \times h$ three plateaus of different hyperfine character $F = 2$, mixed F , and $F = 1$ emerge that form a triplet, doublet, and singlet structure, respectively, in the vicinity of the butterfly crossing at $R \approx 260 a_0$. N and Ω are quantum numbers which label the PECs.

Here, $\vec{S} = \vec{s}_1 + \vec{s}_2$ is the total electronic spin, $\vec{J} = \vec{L} + \vec{S}$, and M_J is the corresponding magnetic quantum number. The interaction strength in each channel depends on the scattering lengths/volumes $a(L, S, J, k) = -k^{-(2L+1)} \tan \delta(L, S, J, k)$, where $\delta(L, S, J, k)$ are phase shifts of an electron with wave number k that scatters off a ^{87}Rb ground state atom. As basis for our simulations we employ phase shift data from [21, 23]. The wave number is calculated via the semiclassical relation $k = \sqrt{2/R - 1/n_{\text{eff}}^2}$. To compute the PECs in the vicinity of the $16P_{1/2}$ state (which represents the closest asymptotic state) we use the effective principle quantum number $n_{\text{eff}} = 13.3447$. The cusps in the outer wells of the PECs, e.g. around $R = 360 a_0$ in Fig 1(b), occur due to the non-analytic behavior of k close to the classical turning point, where k becomes zero.

Since V neither commutes with H_{Ryd} nor with H_{g} , neither \vec{F} nor \vec{j} are conserved quantities. A good quantum number to discriminate the PECs is $\Omega = m_l + m_1 + m_2 + m_l$, which corresponds to the projection of the total angular momentum of the (non-rotating) molecular system on the internuclear axis. Here, m_l, m_1, m_2, m_l are the magnetic quantum numbers of l, s_1, s_2, l , respectively. Due to the axial symmetry of the system, there is energetic degeneracy with respect to $\pm\Omega$.

In general, for the PEC calculations we restrict the Hilbert space to a subset of Rydberg states in a spectral region of interest, as described in Appendix A. Figure 3(a) shows the

PECs from Fig. 1(b) when p -wave interaction is included, i.e. there exist $a(L = 1, S, J, k) \neq 0$. At distances $R < 300 a_0$ the PECs are strongly distorted as compared to the pure s -wave approach. This is a consequence of a p -wave shape resonance of the interaction between the P -orbital Rydberg electron and the ground state atom. The resonance occurs at a distance where the collision energy between these two partners is approximately $E_r = 22 \text{ meV}$ [30]. The resonant p -wave interaction gives rise to butterfly PECs [15, 23], which originate from the hydrogenic $n = 14$ manifold and cross through the other Rydberg levels. After the butterfly PECs have crossed the P -orbital PECs at a distance of $R \approx 250 a_0$ they steeply go down to energies of about -100 to $-500 \text{ GHz} \times h$ before they bend over due to level repulsion with the lower $n = 13$ hydrogenic manifold [see Fig. 3(a)]. There, the butterfly PECs exhibit potential wells which support several bound vibrational states [7].

In our work, we focus on a different region which is shown in Fig. 3(b). It is precisely the part of the P -state PECs of Fig. 1(b) which is most strongly perturbed by the resonant p -wave interaction. The perturbation gives rise to the following three effects: (1) there is a cut-through at the bottom of each potential well; (2) there is strong mixing of hyperfine states (F -mixing); (3) there are additional splittings of the PECs near the avoided crossings. As we will derive in Sec. IV, the angular momentum $\vec{N} = \vec{s}_1 + \vec{s}_2 + \vec{l}$ is useful for labeling the

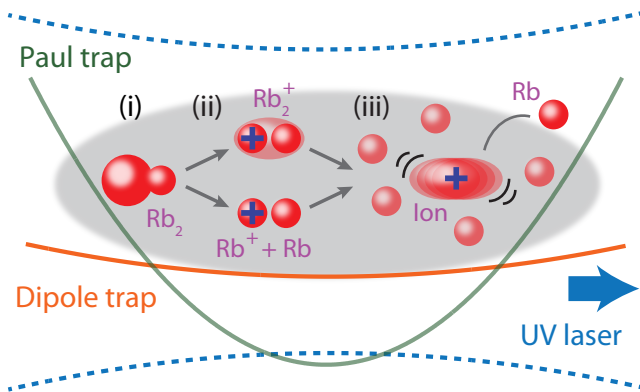


FIG. 4. Illustration of the experimental setup and scheme. The orange solid line indicates the dipole trap potential for the ultracold neutral atoms while the green solid line represents the Paul trap potential for ions. (i) Inside the atom cloud (indicated by the gray colored area) Rb_2 Rydberg molecules are produced by means of the UV photoassociation laser (blue dashed line and blue arrow). (ii) The molecules can decay into ions, where processes leading to Rb^+ and Rb_2^+ are possible, in general [34, 35]. A resulting ion is captured by the Paul trap. (iii) The micromotion-driven ion elastically collides with Rb atoms leading to atom loss from the dipole trap.

PECs, because it provides the correct multiplicity. Strictly speaking, however, N is not a good quantum number. States with dominant $F = 2$ ($F = 1$) content are labeled $N = 5/2$ ($N = 1/2$), respectively, and states with mixed F -character are labeled $N = 3/2$ [see Fig. 3(b)]. Close to the crossing the $N = 5/2$ curve splits up into three components which have the quantum numbers $|\Omega\rangle = \{1/2, 3/2, 5/2\}$. The $N = 3/2$ curve splits up into two components with $|\Omega\rangle = \{1/2, 3/2\}$, while the $N = 1/2$ curve does not split since it only consists of a $|\Omega\rangle = 1/2$ component. Please note that Ω is not the projection quantum number of N . In our experiments, which we will describe in the following, we observe clear signatures of these Ω -splittings.

III. EXPERIMENTS

The experiments are carried out in a hybrid atom-ion setup [31] consisting of a crossed optical dipole trap for an ultracold cloud of ^{87}Rb ground state atoms and a linear Paul trap for detecting Rydberg molecules after ionization. The dipole trap is operated at a wavelength of 1065 nm and has a potential depth of about $20 \mu\text{K} \times k_B$. The atomic sample is either prepared in the hyperfine state $F = 1, m_F = -1$ or in the state $F = 2, m_F = +2$. It has a temperature of $\approx 1 \mu\text{K}$, and typically consists of about 4×10^6 atoms. The cloud is Gaussian-shaped with a size of $\sigma_{x,y,z} \approx (70, 10, 10) \mu\text{m}$ along the three directions of space.

The general procedure of our experiment is illustrated in Fig. 4. In step (i) Rb_2 Rydberg molecules are created by photoassociation using a narrow-linewidth laser with a wavelength of about 302 nm (for technical details on the photoassociation laser setup, see Appendix B). Some of these molecules

decay into ions (ii) which are subsequently trapped in the linear Paul trap with its potential depth of about 1 eV. The Paul trap is centered on the optical dipole trap so that the trapped ions are immersed in the atom cloud. We detect the ions (iii) by measuring the losses they inflict on the atom cloud, as demonstrated in [32, 33]. In brief, the losses are due to micromotion-driven elastic collisions between atoms and ions, which expel atoms out of the shallow dipole trap. Even a single ion can lead to a significant signal. In general, the number of remaining atoms decreases with increasing number of ions. By measuring the atom loss as a function of the frequency of the photoassociation laser light we obtain a spectrum of the molecular Rydberg states.

In Fig. 5 two measured Rydberg photoassociation spectra in the vicinity of the atomic $16P$ Rydberg state are presented. We note that not all of the experimentally observed lines are resolved in these two spectra. The normalized atom loss $L = 1 - \tilde{N}/\tilde{N}_0$ is shown as a function of the frequency of the photoassociation laser light. \tilde{N} is the remaining number of atoms after an experimental run and \tilde{N}_0 is the remaining number of atoms when the photoassociation laser was turned off. The atom numbers are measured via absorption imaging. For the measurements of Fig. 5 the frequency of the photoassociation laser was scanned in steps of 20 MHz, and each data point represents a single run of the experiment. Scan (a) (blue data points) shows data for atoms prepared in the hyperfine state $F = 1, m_F = -1$, while scan (b) (red data points) was obtained for atoms prepared in $F = 2, m_F = +2$. For $F = 1$ samples, the laser frequency ν is given in terms of $\Delta\nu = \nu - \nu_0$, whereas for $F = 2$ samples it is given in terms of $\Delta\tilde{\nu} = \nu - \nu_0 + 2 \times \nu_{\text{hfs}}$. Here, $\nu_0 = 991.55264 \text{ THz}$ is the resonance frequency for the $16P_{1/2}$ atomic Rydberg line when starting with $F = 1, m_F = -1$ atoms, and $\nu_{\text{hfs}} = 6.835 \text{ GHz}$ is the hyperfine splitting of the electronic ground state of ^{87}Rb [28, 36]. The frequency offset difference of $2 \times \nu_{\text{hfs}}$ helps to directly compare positions of molecular resonance lines in the $F = 1$ and $F = 2$ data. Besides the photoassociation signals the spectra also include the $16P_{3/2}$ and $16P_{1/2}$ atomic Rydberg lines which are marked with arrows. A discussion of the atomic lines is given in Appendix C. In the following, we focus on the spectral frequency range of $10 \text{ GHz} < \Delta\nu < 40 \text{ GHz}$, which corresponds to the potential curves shown in Fig. 3(b).

In contrast to the atomic signals, the molecular signals have rather symmetric line shapes with typical linewidths (FWHM) on the order of several tens of MHz. As an example, we show a high resolution scan of a typical molecular line in Fig. 6(i) (blue data) which approximately has the shape of a Gaussian. This particular line is identical to the one labeled with (i) in Fig. 5(a). Without ion trap no photoassociation loss signal is visible in the data of Fig. 6(i) (see flat magenta curve). We note, that the loss-signal strengths in Fig. 5 have a strongly non-linear dependence on the number of trapped ions. While the largest loss signals correspond to hundreds of ions the smallest loss peaks are the result of only a few ions.

A data analysis shows that the measured photoassociation spectra in the range $10 \text{ GHz} < \Delta\nu < 40 \text{ GHz}$ consist of three different vibrational ladders, each with a different multiplet substructure of the vibrational levels. The frequency spacings

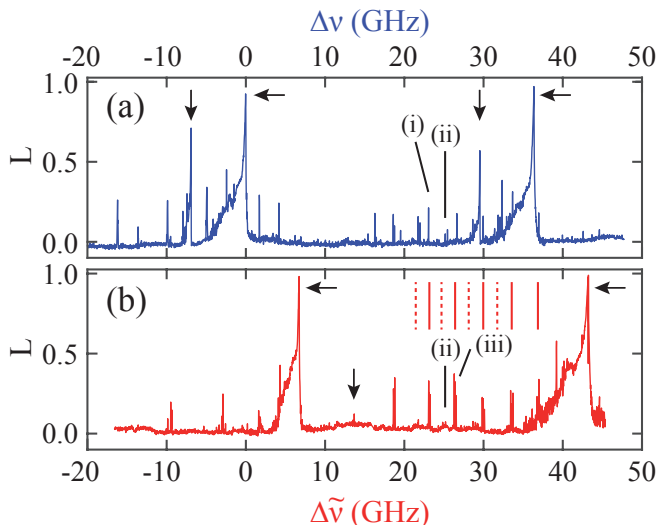


FIG. 5. Spectra measured for atomic samples initially prepared in the hyperfine state $F = 1$ (a) and $F = 2$ (b), respectively. Shown is the atom loss L as a function of the frequency ν of the UV spectroscopy laser light. The frequency ν is provided in terms of $\Delta\nu = \nu - \nu_0$ (a) and $\Delta\tilde{\nu} = \nu - \nu_0 + 2 \times \nu_{\text{hfs}}$ (b), where $\nu_0 = 991.55264$ THz and $\nu_{\text{hfs}} = 6.835$ GHz. For the two spectra, the frequency offsets are chosen to be different by $2 \times \nu_{\text{hfs}}$ in order to vertically line up identical molecular lines. The data of (a) are obtained for a pulse duration of 125 ms of the spectroscopy light while for (b) 200 ms are used (the light intensities, micromotion energies and ion-atom cloud interaction times are about the same for both scans). Here, the horizontal and vertical black arrows mark resonances assigned to atomic transitions. The black solid lines and corresponding denotations (i), (ii), and (iii) indicate multiplet line structures that are investigated in more detail in Fig. 6. The vertical red dashed (red solid) lines illustrate the frequency positions of observed weak (strong) three-line structures for $F = 2$ (see text).

between the vibrational levels of a given ladder are approximately equidistant and typically between 1.4 to 1.8 GHz. The three vibrational manifolds clearly correspond to the PECs characterized by $N = 1/2$, $3/2$, and $5/2$, respectively, as shown in Fig. 3(b). Actually, we find that one of the ladders can only be observed when starting with an ensemble of $F = 2$ atoms. The vertical red solid and dashed lines in Fig. 5(b) indicate measured frequency positions of corresponding vibrational levels. Such a selective behavior is expected for the $N = 5/2$ state according to dipole transition selection rules. Indeed, the substructure of the vibrational levels of this particular manifold is given by line-triplets. This supports the assignment to the $N = 5/2$ state due to its predicted splitting into the components $|\Omega| = \{1/2, 3/2, 5/2\}$. Figure 6(iii) shows such a triplet of lines. The scan represents a high-resolution measurement of the structure (iii) in Fig. 5(b). We observe that the line-triplets generally follow a systematic behavior. The separation between adjacent resonances is typically on the order of about 100 MHz. Furthermore, the splitting between the first and second line is only about $2/3$ of the splitting between the second and the third line. In addition, the signal strength of the third resonance is generally smaller as compared to the

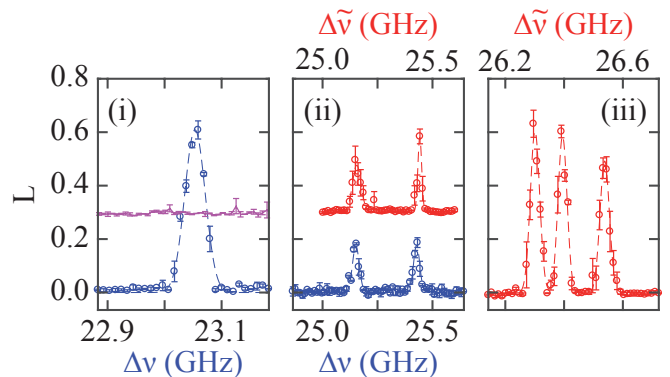


FIG. 6. Multiplet resonance structures observed for atomic samples initially prepared in the hyperfine state $F = 1$ (blue data points) and $F = 2$ (red data points), respectively. In the left panel for the magenta data points the Paul trap was off during the spectroscopy pulse. Here, the pulse duration of the spectroscopy light was 200 ms for the $F = 1$ data and 300 ms for the $F = 2$ data. For better visibility the magenta data points and also the red data points in the center panel are shifted in vertical direction by 0.3. The error bars represent the statistical uncertainty. Dashed blue and red lines are the results of Gaussian fits.

other two resonances which are of similar strength (see also Fig. 9 in the Appendix).

The second one of the three ladders consists of a succession of line-doublets. These levels can be observed both for $F = 2$ as well as $F = 1$ samples. Clearly, this ladder corresponds to the $N = 3/2$ state in Fig. 3(b) which is of mixed F character, and splits up into the components $|\Omega| = \{1/2, 3/2\}$. An example for such a line-doublet is shown in Fig. 6(ii) where measurements for $F = 1$ and $F = 2$ atomic samples are presented. This doublet is found in Figs. 5(a) and (b) at locations (ii). The strengths of line-doublet signals are generally lower for $F = 2$ as compared to $F = 1$ (except for the structure at $\Delta\nu \sim 18.7$ GHz). In fact, some of the line-doublets could only be detected for $F = 1$. Typically, the line splitting within a line-doublet is a few hundred MHz. Finally, the third ladder corresponds to the $N = 1/2$ PEC in Fig. 3(b) which has $|\Omega| = 1/2$. It can only be addressed from $F = 1$ atomic samples. This vibrational manifold consists of a sequence of single lines [see e.g. Fig. 6(i)].

Finally, we note that quite generally for each of the ladders the signal strength strongly alternates between adjacent vibrational levels. In the spectrum of Fig. 5(b) this is indicated by the vertical red solid and dashed lines. Although not visible in Fig. 5(b), in experiments with higher signal-to-noise ratio we observe also the much weaker resonances at the positions of the dashed vertical red lines. How to improve the signal-to-noise ratio is discussed in more detail in Appendix D (corresponding measurements are shown in Fig. 9). The alternation of the signal strength can be explained as a consequence of the change of an approximate g/u symmetry of the vibrational molecular wave function from one vibrational state to another. The excitation rate to a molecular state is proportional to the Franck-Condon factor (see, e.g., [11]). Indeed, for molecular wave functions with g symmetry the Franck-Condon fac-

tors should in general be significantly higher as compared to molecular wave functions with u symmetry. An overview of all measured resonance lines and splittings is given in Tab. II of the Appendix.

IV. SPIN-SPIN AND SPIN-ORBIT INTERACTIONS

In the following, we investigate in detail the reasons for the splitting of the PECs with a given N quantum number into the various Ω components. In particular, we are interested to find out to what extent spin-orbit interaction between the total electronic spin \vec{S} and the orbital angular momentum of the Rydberg electron \vec{L} with respect to the ground state atom (i.e. $\vec{L} \cdot \vec{S}$ coupling) plays a role. To this end, we introduce three control parameters λ_1 , λ_2 , and λ_3 that govern the strengths of the different scattering channels. The mapping is summarized in Table I. When $\lambda_1 = \lambda_2 = \lambda_3 = 0$, the electron-atom interaction V is insensitive to the total electronic spin \vec{S} and the interaction can be simplified to [1, 15, 37]

$$V = 2\pi a_s(k)\delta(\vec{R} - \vec{r}) + 6\pi a_p(k)\overleftarrow{\nabla}_{\vec{r}} \cdot \delta(\vec{R} - \vec{r})\overrightarrow{\nabla}_{\vec{r}} \quad (3)$$

with $a_s(k) = a(0, 1, 1, k)$, $a_p(k) = a(1, 1, 1, k)$, and $\vec{R} = R\hat{e}_z$. Figure 7 shows that for this case there is no splitting of the PECs for either one of the $F = 1, 2$ branches. We now turn on λ_1 , while keeping $\lambda_2 = \lambda_3 = 0$. The parameter λ_1 changes the singlet s -wave interaction away from the value of the triplet s -wave interaction. As a consequence a splitting of each of the $F = 1, 2$ branches is obtained in Fig. 7. This splitting can also be directly observed in the PECs of Fig. 1(b) at distances $\lesssim 370 a_0$. Each asymptote breaks up into two oscillatory PECs, marked with A and B. There is an additional, non-oscillatory PEC, marked with C, for each $P_{3/2}$ asymptote. These C PECs correspond to Rydberg states with $m_j = \pm 3/2$ which do not undergo s -wave interaction, because the ground state atom on the z -axis is located at the node of the $|m_l| = 1$ electronic orbital. The remaining interaction of the C PECs in Fig. 1(b) is then solely through the attractive $1/R^4$ polarization potential due to the Rb^+ ionic core.

In the literature [9, 12, 18, 19] each pair of oscillatory PECs is subclassified into a 'deeper' curve (A) and a 'shallower' curve (B). The deeper curves correspond in Fig. 7 to the lines which are flat as a function of λ_1 . They are flat because they are insensitive to the singlet s -wave interaction. However, the deeper curves are not pure triplet states due to Rydberg fine structure. We explain how this is possible with the following example. We consider the electronic state of a Rydberg atom in a P state with total orbital angular momentum $j = 1/2$ and projection $m_j = 1/2$ and a ground state atom in a polarized nuclear spin state $F = 2$ and $m_F = 2$,

$$\left(\begin{array}{c} \psi_{m_l=0,\uparrow}(\vec{r}) \\ \psi_{m_l=1,\downarrow}(\vec{r}) \end{array} \right) \otimes |F = 2, m_F = 2\rangle. \quad (4)$$

To first order perturbation theory (with respect to weak s - and p -wave interaction) this state must be an eigenstate of the Hamiltonian, as it is the only possible realization of an

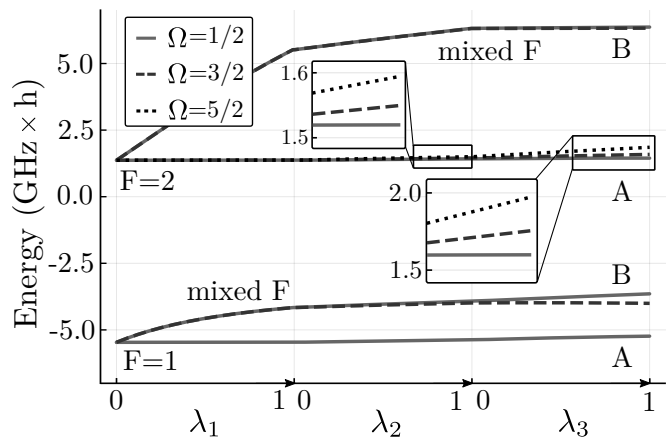


FIG. 7. PEC values of the $16P_{1/2}$ state at $R = 300 a_0$ as a function of the interaction control parameters $\lambda_{1,2,3}$ (see also Tab. I). On the left, where $\lambda_1 = \lambda_2 = \lambda_3 = 0$, interaction is identical for singlet and triplet states. s -wave and p -wave interactions are, however, not identical. When going to the right λ_1 , λ_2 , and λ_3 are subsequently turned on. Parameter λ_1 changes the singlet s -wave interaction which leads to a splitting of the lines. While the unshifted states keep their F quantum number, the split-off ones exhibit mixing of $F = 1$ and $F = 2$. Parameter λ_2 changes the singlet p -wave scattering: Splitting of the Ω -components on the 100 MHz-scale is introduced. Parameter λ_3 introduces a $\vec{L} \cdot \vec{S}$ type of interaction: The Ω -splitting is significantly enhanced.

$\Omega = 5/2$ state in the Hilbert subspace considered here. The spin-up component has $m_l = 0$ and the spin-down component has $m_l = 1$. Together with the spin-stretched ground state atom, the spin-up component forms a pure spin triplet. Therefore, this component does not interact in the s -wave singlet channel. The spin-down component is a mixed singlet/triplet state. However, it still does not interact in the s -wave singlet channel because $m_l = 1$ and hence the ground state atom is located at the node of the electronic wave function. Thus, despite the fact that the state of Eq. (4) has a singlet component, it is insensitive to s -wave singlet interaction.

The state of Eq. (4) is just one example for the many degenerate eigenstates associated with the deep PECs. The degeneracy of the deep and shallow PECs can be obtained with the help of the spin operator \vec{N}^2 , where $\vec{N} = \vec{S} + \vec{I} = \vec{s}_1 + \vec{F}$. \vec{N}^2 does not commute with H_{Ryd} due to the Rydberg fine structure, however, it is still useful for labeling the scattering channels, as we show in the following. The basis states of a given F -branch all have a similar form as the state in Eq. (4). Within the vector space spanned by these basis states, we want to determine the dimension of the subspace that is susceptible to singlet s -wave interaction. Since the $|m_l| = 1$ component of a basis state does not contribute to s -wave interaction, we only consider its $m_l = 0$ component, of which the spin can be up or down. Thus, the problem can be reduced to determining the dimension of the formed $S = 1$ subspace when coupling an electronic spin \vec{s}_1 to the angular momentum F manifold where $\vec{F} = \vec{I} + \vec{s}_2$. For this, we divide up the resulting new manifold into subspaces with good quantum number N . Since \vec{N}^2 commutes with both \vec{S}^2 and \vec{F}^2 , this will help us sorting

scattering channel		model	mapping
s -wave ($L = 0$)	singlet ($S = 0$)	$J = 0$	λ_1 $a(0,0,0,k) \mapsto \lambda_1 a(0,0,0,k) + (1 - \lambda_1) a(0,1,1,k)$ $a(0,1,1,k) \mapsto a(0,1,1,k)$
	triplet ($S = 1$)	$J = 1$	
p -wave ($L = 1$)	singlet ($S = 0$)	$J = 1$	λ_2 $a(1,0,1,k) \mapsto \lambda_2 a(1,0,1,k) + (1 - \lambda_2) a(1,1,1,k)$ $a(1,1,0,k) \mapsto \lambda_3 a(1,1,0,k) + (1 - \lambda_3) a(1,1,1,k)$
		$J = 0$	
	triplet ($S = 1$)	$J = 1$	λ_3 $a(1,1,1,k) \mapsto a(1,1,1,k)$ $a(1,1,2,k) \mapsto \lambda_3 a(1,1,2,k) + (1 - \lambda_3) a(1,1,1,k)$
		$J = 2$	

TABLE I. Overview of the scattering lengths/volumes $a(L, S, J, k)$ that are modified via control parameters λ_1 , λ_2 , and λ_3 in order to study the splitting mechanism in Fig. 7.

out the spin structure. We note, however, that \vec{S}^2 and \vec{F}^2 do not commute. For $F = 2$, N can be $N = 5/2$ or $N = 3/2$. Since the $N = 5/2$ subspace must have $S = 1$ it belongs to branch A. With the help of Wigner $6j$ coefficients one can show that the $N = 3/2$ subspace, however, contains states with singlet and triplet character and therefore belongs to branch B. Similarly, for $F = 1$, we have the subspaces $N = 3/2$ and $N = 1/2$. $N = 1/2$ goes along with $S = 1$ and thus belongs to branch A, whereas $N = 3/2$ includes both S characters and belongs to branch B. As the difference in the singlet and triplet s -wave interactions becomes larger, the two $N = 3/2$ manifolds of the $F = 1$ and $F = 2$ branches start mixing. The degree of F -mixing depends on the relative strength of the differential singlet/triplet s -wave interaction and the hyperfine interaction H_g . The F -mixing due to the presence of a singlet s -wave scattering channel is essential for the spin flip effect observed in [8]. N reproduces the multiplicities for the PECs, which are visible in Fig. 3 (b) and Fig. 7: For the $F = 2$ asymptote, the deep curve corresponds to $N = 5/2$ and has six degenerate states of pure $F = 2$ character. For the $F = 1$ asymptote, the deep curve corresponds to $N = 1/2$ and has two degenerate states of pure $F = 1$ character. The shallow curves of both, the $F = 1$ and the $F = 2$ asymptote correspond to $N = 3/2$ and have four degenerate states of mixed $F = 1$ and $F = 2$ character each. While this regime of interactions is sufficient to describe the PECs at the outer potential wells (in this case for $R > 300 a_0$), additional p -wave related interactions become important for smaller internuclear separations and will be relevant in the next parameter regime of control parameters.

The next regime is $\lambda_1 = 1$, $\lambda_2 > 0$, and $\lambda_3 = 0$ (see Fig. 7). The parameter λ_2 introduces a difference between the singlet and triplet channels for p -wave scattering, essentially corresponding to a spin-spin interaction. This affects in particular the spinor components with $m_l = \pm 1$, which only probe the p -wave interaction but not the s -wave interaction, and introduces additional splittings.

Although the state with $\Omega = 5/2$ of Eq. (4) is of pure triplet character in its $m_l = 0$ component, it is of mixed singlet/triplet character in its $m_l = 1$ component, as discussed before. As a consequence, it will experience a first order level shift. States with a different $|\Omega|$ have different mixing ratios and will exhibit different shifts. Therefore, the spin-selective p -wave interaction generally leads to a splitting of $|\Omega|$ states. This splitting, however, arises only due to the Rydberg fine structure and is, hence, not visible in S -state ultralong-range Rydberg molecules recently studied [38], since they do not exhibit such a fine structure.

Finally, for the regime $\lambda_1 = \lambda_2 = 1$, $\lambda_3 > 0$ the full interaction introduced in Eq. (2) is realized by including the J -dependency of the p -wave triplet scattering. The physical origin of the J -dependency is $\vec{L} \cdot \vec{S}$ spin-orbit coupling. Each J -channel ($J = \{0, 1, 2\}$) is associated with a characteristic energy E_r^J where the p -wave shape resonance occurs. For our scattering phase shifts these values are $E_r^{J=0} = 19.21$ meV, $E_r^{J=1} = 20.42$ meV, and $E_r^{J=2} = 23.22$ meV [21, 30]. Thus, electronic triplet states of different J experience different interaction strength for any given internuclear separation, which leads to additional splitting of the PECs. In Fig. 7, this splitting is on the order of a few hundred MHz for the lower mixed F branch around $-4 \text{ GHz} \times h$ and the $F = 2$ branch around $2 \text{ GHz} \times h$. It is much larger than the splitting due to p -wave λ_2 spin-spin interaction. The calculated splitting is of the right size to explain our experimentally observed multiplet splittings which are also around a few hundred MHz (see also Fig. 6). This shows the crucial role that $\vec{L} \cdot \vec{S}$ coupling can play for the multiplet line structures. However, we need to point out, that the results in Fig. 7 are calculated for one specific internuclear separation of $R = 300 a_0$, since the PECs at this distance are well suited for illustrating the different splitting mechanisms. In general, the $|\Omega|$ -splittings depend on R due to the energy dependence of the scattering lengths/volumes $a(L, S, J, k)$ as well as the spatial variation of the Rydberg electron wave function. Therefore, at other locations the $|\Omega|$ -splittings could be dominated by the λ_2 spin-spin interaction while $\vec{L} \cdot \vec{S}$ interaction is of minor importance. Consequently, both splitting mechanisms can potentially explain the observed multiplet structures [39]. Discriminating the impact of both effects on vibrational energies in a fully quantitative way is, however, challenging due to the following uncertainties of the model: (1) incomplete knowledge of the electron-atom interaction which is here modeled by *ab initio* phase shifts; (2) possible breakdown of the Born-Oppenheimer approximation due to avoided crossings of the PECs; (3) limited accuracy due to convergence issues inherent to the pseudopotential approach [21, 40]. To resolve this, an extended experimental and theoretical investigation is necessary.

V. ADIABATIC VERSUS NON-ADIABATIC DYNAMICS

In Figure 8 we show the measured vibrational ladders (red lines) for the states $N = \{1/2, 3/2, 5/2\}$ together with their

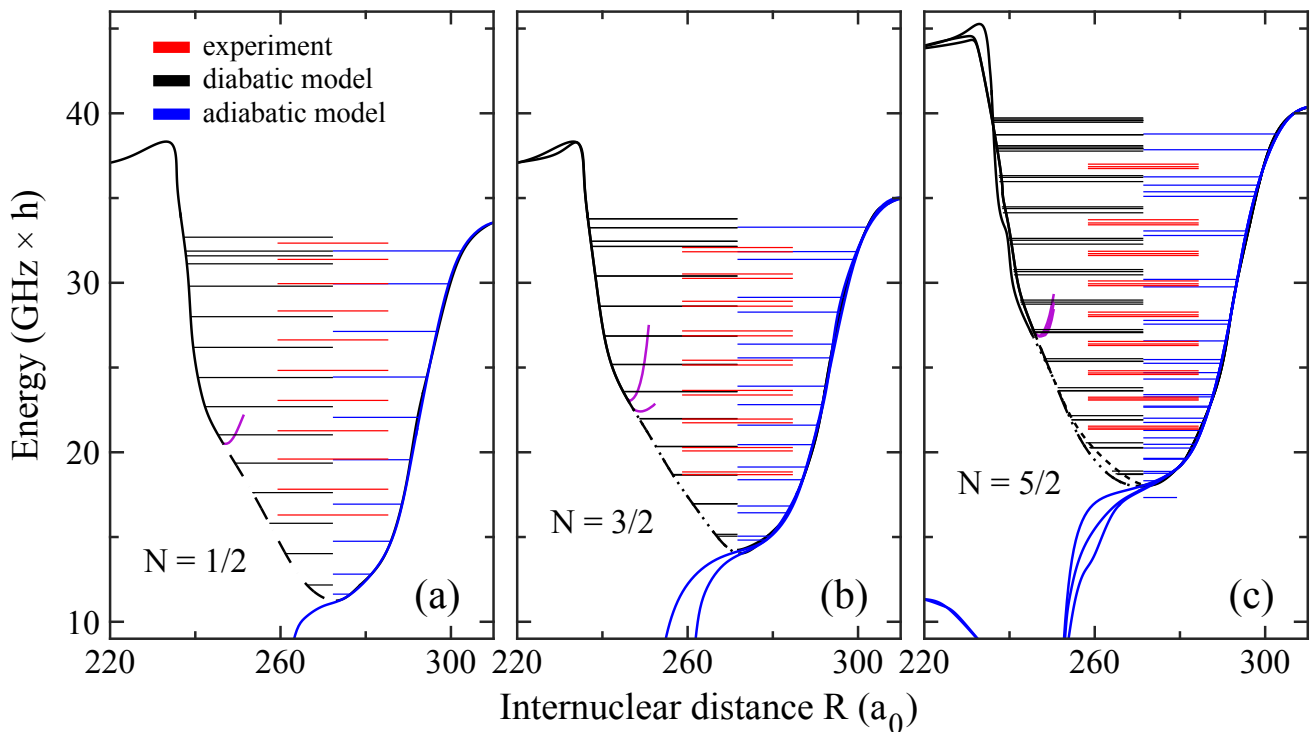


FIG. 8. Comparison of measured molecular term energies (red horizontal lines) and calculated molecular term energies using either an adiabatic approach (blue horizontal lines) or a diabatic approach (black horizontal lines). The PECs for the different states $N = 1/2$ (a), $N = 3/2$ (b), and $N = 5/2$ (c) correspond to the ones of Fig. 3. For the adiabatic approach only the blue PECs are used. The dashed black lines indicate how the potential gaps are closed for the diabatic calculations (see text for more details). Numerical values for the term energies can be found in Tab. II.

respective PECs [see also, e.g., Fig. 3(b)]. In view of the cut-through at the bottom of each potential well due to the avoided crossing of the butterfly state the question arises how these vibrational bound states come about since there is no apparent confinement. In the following we discuss two limiting scenarios for this.

In the adiabatic scenario, sufficient confinement is achieved due to quantum reflection of the wave function at the steep drop of the PEC on the left hand side of the ledge at an internuclear distance of about $260 a_0$. Such quantum reflection states [17, 18] have been previously observed for ultralong-range Rydberg molecules [17]. In the non-adiabatic scenario the dynamics of the vibrational motion at the avoided crossing is fast enough so that the molecule non-adiabatically passes through and thus is confined by the original potential well. We have carried out calculations for both scenarios and show the obtained vibrational ladders in Fig. 8. The blue (black) horizontal lines correspond to the adiabatic (non-adiabatic) scenario. In addition, we list the calculated term frequencies and level splittings in Tab. II of the Appendix.

Regarding the adiabatic approach (blue PECs in Fig. 8) the positions and lifetimes of the respective resonances are obtained in terms of the phase Θ of the complex reflection coefficient of an outgoing plane wave reflected at the potential curve. A molecular state is found at energies E , at which the phase Θ undergoes a sudden change. According to Wigner's time delay interpretation, the corresponding lifetime equals

$\tau = \frac{\hbar}{2} \frac{d\Theta}{dE}$ [41]. In the diabatic approach the gap at the left side of each potential well in Fig. 3(b) is essentially ignored. To carry out numerical calculations, we first connect two adiabatic PECs at the avoided crossing to close the gap. For this a spline interpolation is used, and the obtained PECs are shown as black curves in Fig. 8 (dashed parts approximately represent the bridged gaps). The bound states in the resulting potential wells are obtained by solving the 1D Schrödinger equation with standard methods. Within this approach, decay of such states is neglected. We note that the calculated results depend on the details of the interpolations of the PECs. Our particular choice of spline interpolations is to some extent arbitrary.

Qualitatively, the calculations using the adiabatic approach are in agreement with the observed multiplicities of resonance lines and the approximate shapes of the vibrational ladders. However, quantitatively there are discrepancies, e.g. when considering the splittings within individual multiplet line structures. For the $N = 3/2$ line-doublets and the $N = 5/2$ line-triplets the calculated spacings between the $|\Omega\rangle$ components are generally too large. Concerning the vibrational splittings there is rough agreement (within a factor of two) between measured and calculated values for the states $N = 1/2$ and $N = 3/2$. Furthermore, close inspection shows that the predicted two lowest vibrational levels are not observed in the experiment. This could indicate that the computed potential depths are too large by a few GHz, which is within the typical uncertainties of the perturbative electronic structure calcula-

tions [21, 40]. Finally, from the adiabatic approach we expect resonance linewidths on the order of 100 to 400 MHz for the molecular levels while in the experiment these are typically only about several tens of MHz. Therefore, the measurements can just partially be explained when assuming full adiabaticity.

Using the diabatic approach, the overall agreement between the calculations and the experiment is better than for the adiabatic approach. In particular, the predicted vibrational level spacings are close to the observed values. Apart from that the calculated multiplet splittings are too small. Furthermore, similar as for the adiabatic scenario, there are two vibrational bound states below the lowest experimentally observed levels. An alternative explanation for this, besides the one that the computed potentials are too deep, could be that the two lowest bound states exhibit such short lifetimes that their resonance lines are too broad to be detected. Because of the comparatively low kinetic energy at the crossing the diabatic behavior might break down for these two levels.

A realistic description of the ultralong-range Rydberg molecular bound states probably lies in between the discussed limiting cases of adiabaticity and diabaticity. Although the diabatic model overall fits better to describe the observed spectra, some amount of adiabaticity at the avoided crossings is needed to couple out flux for the ion signals.

We expect that an improved agreement between theory and experiment can be achieved by performing full vibronic structure investigations that take into account non-adiabatic couplings between PECs. However, due to the complexity of the system considered here, which exceeds significantly those of standard vibronic coupling problems for energetically low-lying molecular states [42], a full vibronic structure investigation is beyond reach for the present work. In addition, it might turn out that the effective pseudopotential of Eq. (2) might be not adequate to fully describe all relevant interactions.

VI. CONCLUSIONS

In conclusion, we have studied ultralong-range Rydberg molecules in a previously unexplored parameter regime for which the energy level structure is determined by the interplay of spin-spin and spin-orbit interactions, as well as s - and p -wave electron-atom scattering. We experimentally observe that the molecular level structure consists of various vibrational ladders, each with a characteristic substructure of level singlets, doublets, and triplets. Using a Fermi model we can explain these line multiplicities and assign spin quantum numbers to the levels. However, our quantitative analysis of the experimental data indicates the necessity of a much more elaborate modeling which goes beyond the Born-Oppenheimer approximation and which includes a more accurate description of the involved electronic interactions.

We expect our work to spark increased theoretical efforts to explain the subtle interaction effects in Rydberg molecules which become apparent in energy level structures that can have even higher complexity than the ones studied here. In future work, it will be important to extend our studies to Ryd-

berg molecular states with principal quantum numbers in the vicinity of $n = 16$. For such low principal quantum numbers the shapes of the PECs of the p -wave ultralong-range Rydberg molecular states vary strongly, since the crossings with the butterfly states occur at different locations for different n . Therefore, also the relative and absolute strengths of spin-spin and spin-orbit coupling mechanisms are considerably changing with n . An enlarged data set will then help to establish a consistent theoretical description of the internal Rydberg interactions, and in particular, to extract the role of the $\vec{L} \cdot \vec{S}$ coupling in detail.

In the future, these experiments can be further complemented by investigating molecular $S_{1/2}$ Rydberg states instead of $P_{1/2}$ and $P_{3/2}$ states. Since for $S_{1/2}$ states the $\vec{l} \cdot \vec{s}_1$ coupling only has a minor impact, we can identify $\vec{L} \cdot \vec{S}$ coupling effects in a direct way. Additionally, it has been proposed to employ homogeneous weak magnetic fields to verify the $\vec{L} \cdot \vec{S}$ coupling by aligning $S_{1/2}$ state dominated Rydberg molecules [38].

ACKNOWLEDGMENTS

We thank Herwig Ott for valuable discussions. This work was supported by the German Research Foundation (DFG) within the priority program "Giant Interactions in Rydberg Systems" [DFG SPP 1929 GiRyd (projects HE 6195/3-1, PF 381/17-1, and SCHM 885/30-1)], and under DFG project PF 381/13-1. M.D. acknowledges support from Universität Ulm and Ulmer Universitätsgesellschaft (UUG) through a Forschungsbonus grant. F.M. acknowledges support from the Carl-Zeiss foundation and is indebted to the Baden-Württemberg Stiftung for financial support by the Eliteprogramm for postdocs.

APPENDIX

A. Restricting the Hilbert space for numerical calculations

The Hamiltonian H is constructed in a finite basis set that includes the $16S$, $17S$, $15P$, $16P$, $14D$, $15D$ states, and the hydrogenic states with higher orbital angular momenta $l \geq 3$ with principle quantum numbers $n = 13$ and $n = 14$. All these states are considered with all possible total angular momenta j , while the projections m_j are truncated to include $|m_j| \leq 3/2$. According to the choice of the molecular axis lying on the z -axis, states with $|m_j| > 3/2$ do not interact with the ground state atom. Additionally, the ground state atom nuclear and electronic spin are taken into account completely ($m_l = \{\pm 1/2, \pm 3/2\}$ and $m_s = \pm 1/2$). Note, that placing the perturber onto the z -axis significantly reduces the basis set. Since the scattering interaction V vastly exceeds the Zeeman energy for any magnetic fields occurring due to the experimental setup, the atomic orbitals align along the internuclear axis. This is different, however, when the interaction with an external field is comparable or larger than the scattering interaction [10]. An alternative approach to derive the PECs that

circumvents a finite basis set are Green's function methods employed for example in [16, 23]. However, these approaches do not incorporate hyperfine interactions that are crucial for the interpretation of our results.

B. Photoassociation setup

The photoassociation laser operates at wavelengths of around 302 nm. The laser light is generated by a frequency-doubled cw dye laser with a narrow short-time linewidth of a few hundred kilohertz. The laser is frequency-stabilized to a wavelength meter (High Finesse WS7) which is repeatedly calibrated to an atomic ^{87}Rb reference signal at a wavelength of 780 nm in intervals of hours. We achieve a shot-to-shot frequency stability of below ± 10 MHz for the 302 nm light.

A multi mode optical fiber is used to transfer the UV light to the experimental table. At the location of the atoms the spectroscopy beam has a waist ($1/e^2$ radius) of about 1.5 mm and the power is typically in the range of 4 to 10 mW. The light pulse has a rectangular shape and the atoms are exposed to the laser radiation for a duration on the order of 0.1 to 1 s.

C. Atomic lines

The strong resonance lines marked with horizontal black arrows in the spectra (a) and (b) of Fig. 5 correspond to the atomic transitions towards $16P_{1/2}$ and $16P_{3/2}$. Here, the atom loss of the atomic cloud is close to 100%. The $16P_{1/2}$ line is located at $\Delta\nu = 0$ in (a) and at $\Delta\tilde{\nu} \approx \nu_{\text{hfs}} = 6.835$ GHz in (b) which corresponds to the ground state hyperfine splitting. For the excited Rydberg P state the hyperfine splitting can be neglected. The asymmetric tail on the red side of each atomic resonance line arises from the Stark effect due to the electric fields of both the Paul trap and the trapped ions (see also [43–45]). The strong resonance lines marked with vertical black arrows in the spectra (a) and (b) of Fig. 5 also correspond to transitions towards the atomic $16P_{1/2}$ and $16P_{3/2}$ states. These lines are shifted by about $\pm \nu_{\text{hfs}}$ relative to the atomic resonance lines marked with horizontal black arrows. Apparently, each of the prepared $F = 1$ ($F = 2$) samples is not 100% pure but contains a fraction of atoms in the other spin state $F = 2$ ($F = 1$), respectively. Although these admixed fractions are possibly on the percent level or less they still can give rise to large signals due to the non-linear behavior of the atomic loss, as discussed in the main text.

D. Mining of experimental data

In general, we have various parameters available to tune signal strengths for the detection of ultralong-range Rydberg molecules. These are the intensity and pulse duration of the spectroscopy light, but also the ionic micromotion energy and the interaction time between trapped ions and neutral atoms. Figure 9 shows how signals change when we vary these parameters, as indicated by different line colors and scan ranges.

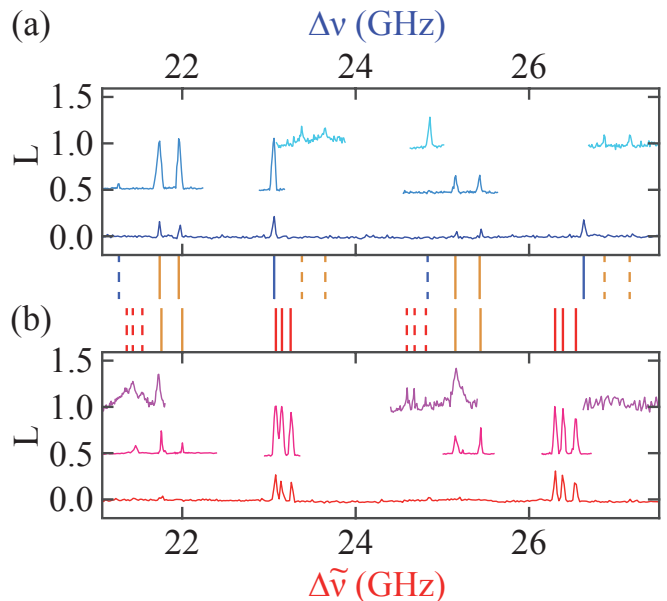


FIG. 9. Measured series of line-multiplets for atomic samples initially prepared in the hyperfine state $F = 1$ (a) and $F = 2$ (b). The blue and red data curves are the same as in Fig. 5. All other spectra are obtained for individually optimized experimental parameters to locally increase the signal-to-noise ratio. For better visibility light blue and magenta data (cyan and purple data) are shifted in vertical direction by 0.5 (1.0). Blue, orange, and red vertical lines on the bottom of plot (a) [on the top of plot (b)] indicate the frequency positions of measured resonances belonging to line-singlets, line-doublets, and line-triplets, respectively. The alternating signal strength behavior for each multiplet series is illustrated by the line style, where solid (dashed) lines represent strong (weak) signals.

The dark blue data in (a) and the red data in (b) are zooms into Fig. 5(a) and (b), respectively. Additional resonance lines which are not visible in these two spectra, can be revealed after individual parameter optimization. The blue, orange, and red vertical lines represent the center frequency positions of the measured resonances of line-singlets, line-doublets, and line-triplets. Solid and dashed vertical lines mark strong and weak signals, respectively. They alternate between adjacent vibrational states for each of the three observed ladders. Within the given frequency range we observe almost the complete series of expected resonances for each multiplet structure. Only the weak line-doublets for $F = 2$ in Fig. 9(b) are missing (see purple data scan at around $\Delta\tilde{\nu} = 27$ GHz).

TABLE II: Measured and calculated molecular energy level positions. The subscripts e, ta, and td denote results from the experiments and the adiabatic and diabatic model, respectively. Δv_e and $\Delta \tilde{v}_e$ are measured resonance frequencies. Δv_{ta} and Δv_{td} give computed term frequencies (referenced to the calculated $5S_{1/2} + 16P_{1/2}$ dissociation threshold). The subscript s indicates splittings between Ω states within individual multiplet structures. The subscript v marks vibrational splittings, which are calculated using the energetically lowest states of two subsequent corresponding multiplet structures. $\delta v_{s,ta}$ and $\delta v_{v,ta}$ are not provided for the triple-line pattern ($N = 5/2$), since using the adiabatic approach no clear series of triple-line structures is obtained. The signal strengths of measured resonance lines are classified in weak (*w*) or strong (*s*). For better comparison the results of the diabatic model calculations are only given for the energy ranges from about the lowest to the highest given experimental resonance positions. Here, n.o. stands for not-observed lines. Values of Δv_e indicated by (*) characterize experimental signals which might come from different molecular states than considered here. The resonance at $\Delta \tilde{v}_e = 31.86$ GHz marked with (**) is rather broad and expected to consist of a $N = 5/2$ and a $3/2$ molecular line which cannot be resolved. We just give this frequency for the corresponding lines of the double- as well as the triple-line pattern.

exp. ($F = 1$)				exp. ($F = 2$)				theo. (adiabatic)			theo. (diabatic)				
Δv_e (GHz)	$\delta v_{s,e}$ (GHz)	$\delta v_{v,e}$ (GHz)	signal strength	$\Delta \tilde{v}_e$ (GHz)	$\delta \tilde{v}_{s,e}$ (GHz)	$\delta \tilde{v}_{v,e}$ (GHz)	signal strength	$ \Omega $	Δv_{ta} (GHz)	$\delta v_{s,ta}$ (GHz)	$\delta v_{v,ta}$ (GHz)	$ \Omega $	Δv_{td} (GHz)	$\delta v_{s,td}$ (GHz)	$\delta v_{v,td}$ (GHz)
vibrational ladder of single lines ($N = 1/2$, pure triplet)															
16.30			<i>s</i>					0.5	11.63			0.5	15.81		
17.82		1.52	<i>w</i>					0.5	12.81		1.18	0.5	17.62		1.81
19.60		1.78	<i>s</i>					0.5	14.75		1.94	0.5	19.36		1.74
21.27		1.67	<i>w</i>					0.5	16.94		2.19	0.5	21.03		1.67
23.06		1.79	<i>s</i>					0.5	19.56		2.62	0.5	22.69		1.66
24.83		1.77	<i>w</i>					0.5	22.06		2.50	0.5	24.41		1.72
26.63		1.80	<i>s</i>					0.5	24.44		2.38	0.5	26.19		1.78
28.34		1.71	<i>w</i>					0.5	27.13		2.69	0.5	28.00		1.81
29.95		1.61	<i>s</i>					0.5	29.94		2.81	0.5	29.80		1.80
31.38*		1.43	<i>w</i>					0.5	31.88		1.94	0.5	31.12		1.32
32.34*		0.96	<i>s</i>									0.5	31.59		0.47
												0.5	31.87		0.28
												0.5	32.69		0.82
double-line pattern ($N = 3/2$, mixed singlet/triplet)															
18.68			<i>s</i>	18.64			<i>s</i>	0.5	14.82			1.5	18.65		
18.84	0.16		<i>s</i>	18.80	0.16		<i>s</i>	1.5	15.05	0.23		0.5	18.69	0.04	
20.08		1.40	<i>w</i>	20.12		1.48	<i>w</i>	0.5	16.43		1.61	1.5	20.33		1.68
20.28	0.20		<i>w</i>	20.32	0.20		<i>w</i>	1.5	16.83	0.40		0.5	20.35	0.02	
21.74		1.66	<i>s</i>	21.76		1.64	<i>s</i>	0.5	18.38		1.95	1.5	21.97		1.64
21.96	0.22		<i>s</i>	22.00	0.24		<i>s</i>	1.5	19.13	0.75		0.5	21.99	0.02	
23.38		1.64	<i>w</i>	n.o.				0.5	20.45		2.07	1.5	23.57		1.60
23.65	0.27		<i>w</i>	n.o.				1.5	21.60	1.15		0.5	23.59	0.02	
25.15		1.77	<i>s</i>	25.15			<i>s</i>	0.5	22.81		2.36	1.5	25.17		1.60
25.43	0.28		<i>s</i>	25.44	0.29		<i>s</i>	1.5	23.90	1.09		0.5	25.19	0.02	
26.87		1.72	<i>w</i>	n.o.				0.5	25.57		2.76	1.5	26.85		1.68
27.16	0.29		<i>w</i>	n.o.				1.5	26.38	0.81		0.5	26.87	0.02	
28.62		1.75	<i>s</i>	28.65			<i>s</i>	0.5	28.27		2.70	1.5	28.61		1.76
28.91	0.29		<i>s</i>	28.93	0.28		<i>s</i>	1.5	29.14	0.87		0.5	28.62	0.01	
30.26		1.64	<i>w</i>	n.o.				0.5	31.38		3.11	1.5	30.39		1.78
30.52	0.26		<i>w</i>	n.o.				1.5	31.84	0.46		0.5	30.41	0.02	
31.83		1.57	<i>s</i>	31.86**			<i>s</i>	0.5	33.28		1.90	1.5	32.14		1.75
32.08	0.25		<i>s</i>	32.10	0.24		<i>s</i>					0.5	32.15	0.01	
triple-line pattern ($N = 5/2$, pure triplet)															
				21.36			<i>w</i>	1.5	19.59			0.5	20.25		
				21.43	0.07		<i>w</i>	2.5	19.64			2.5	20.28	0.03	
				21.54	0.11		<i>w</i>	0.5	20.25			1.5	20.56	0.28	
				23.08		1.72	<i>s</i>	1.5	20.47			0.5	21.91		1.66
				23.15	0.07		<i>s</i>	0.5	20.85			2.5	21.92	0.01	
				23.25	0.10		<i>s</i>	2.5	21.29			1.5	22.16	0.24	
				24.59		1.51	<i>w</i>	0.5	21.76			0.5	23.62		1.71
				24.68	0.09		<i>w</i>	1.5	22.01			2.5	23.64	0.02	
				24.81	0.13		<i>w</i>	0.5	22.66			1.5	23.81	0.17	

Continued on next page

TABLE II: Continuation

exp. ($F = 1$)				exp. ($F = 2$)				theo. (adiabatic)			theo. (diabatic)				
Δv_e (GHz)	$\delta v_{s,e}$ (GHz)	$\delta v_{v,e}$ (GHz)	signal strength	$\Delta \tilde{v}_e$ (GHz)	$\delta \tilde{v}_{s,e}$ (GHz)	$\delta \tilde{v}_{v,e}$ (GHz)	signal strength	$ \Omega $	Δv_{ta} (GHz)	$\delta v_{s,ta}$ (GHz)	$\delta v_{v,ta}$ (GHz)	$ \Omega $	Δv_{td} (GHz)	$\delta v_{s,td}$ (GHz)	$\delta v_{v,td}$ (GHz)
				26.30		1.71	<i>s</i>	1.5	22.72			0.5	25.36		1.74
				26.39	0.09		<i>s</i>	2.5	23.27			2.5	25.37	0.01	
				26.54	0.15		<i>s</i>	0.5	23.40			1.5	25.52	0.15	
				28.01		1.71	<i>w</i>	0.5	24.32			2.5	27.06		1.70
				28.11	0.10		<i>w</i>	1.5	24.70			0.5	27.11	0.05	
				28.27	0.16		<i>w</i>	0.5	25.25			1.5	27.24	0.13	
				29.83		1.82	<i>s</i>	2.5	25.47			2.5	28.74		1.68
				29.94	0.11		<i>s</i>	1.5	26.57			0.5	28.86	0.12	
				30.11	0.17		<i>s</i>	1.5	27.56			1.5	28.98	0.12	
				31.61		1.78	<i>w</i>	2.5	27.78			2.5	30.47		1.73
				31.72	0.11		<i>w</i>	1.5	29.76			0.5	30.66	0.19	
				31.86**	0.14		<i>w</i>	2.5	30.20			1.5	30.78	0.12	
				33.42		1.81	<i>s</i>	2.5	32.79			2.5	32.28		1.81
				33.53	0.11		<i>s</i>	1.5	33.06			0.5	32.51	0.23	
				33.72	0.19		<i>s</i>	0.5	35.10			1.5	32.62	0.11	
				n.o.				2.5	35.37			2.5	34.13		1.85
				n.o.				1.5	35.76			0.5	34.38	0.25	
				n.o.				1.5	36.25			1.5	34.48	0.10	
				36.74			<i>s</i>	2.5	37.85			2.5	35.97		1.84
				36.85	0.11		<i>s</i>	2.5	38.78			0.5	36.22	0.25	
				37.00	0.15		<i>s</i>					1.5	36.32	0.10	
												2.5	37.77		1.80
												0.5	37.92	0.15	
												1.5	37.92	0.00	

- [1] C. H. Greene, A. S. Dickinson, and H. R. Sadeghpour, Phys. Rev. Lett. **85**, 2458 (2000).
- [2] V. Bendkowsky, B. Butscher, J. Nipper, J. P. Shaffer, R. Löw, and T. Pfau, Nature **458**, 1005 (2009).
- [3] J. P. Shaffer, S. T. Rittenhouse, and H. R. Sadeghpour, Nat. Commun. **9**, 1965 (2018).
- [4] W. Li, T. Pohl, J. M. Rost, S. T. Rittenhouse, H. R. Sadeghpour, J. Nipper, B. Butscher, J. B. Balewski, V. Bendkowsky, R. Löw, and T. Pfau, Science **334**, 1110 (2011).
- [5] J. Tallant, S. T. Rittenhouse, D. Booth, H. R. Sadeghpour, and J. P. Shaffer, Phys. Rev. Lett. **109**, 173202 (2012).
- [6] D. Booth, S. T. Rittenhouse, J. Yang, H. R. Sadeghpour, and J. P. Shaffer, Science **348**, 99 (2015).
- [7] T. Niederprüm, O. Thomas, T. Eichert, C. Lippe, J. Pérez-Ríos, C. H. Greene, and H. Ott, Nat. Commun. **7**, 12820 (2016).
- [8] T. Niederprüm, O. Thomas, T. Eichert, and H. Ott, Phys. Rev. Lett. **117**, 123002 (2016).
- [9] D. A. Anderson, S. A. Miller, and G. Raithel, Phys. Rev. Lett. **112**, 163201 (2014).
- [10] A. T. Krupp, A. Gaj, J. B. Balewski, P. Ilzhöfer, S. Hofferberth, R. Löw, T. Pfau, M. Kurz, and P. Schmelcher, Phys. Rev. Lett. **112**, 143008 (2014).
- [11] B. J. DeSalvo, J. A. Aman, F. B. Dunning, T. C. Killian, H. R. Sadeghpour, S. Yoshida, and J. Burgdörfer, Phys. Rev. A **92**, 031403(R) (2015).
- [12] H. Saßmannshausen, F. Merkt, and J. Deiglmayr, Phys. Rev. Lett. **114**, 133201 (2015).
- [13] M. A. Bellos, R. Carollo, J. Banerjee, E. E. Eyler, P. L. Gould, and W. C. Stwalley, Phys. Rev. Lett. **111**, 053001 (2013).
- [14] K. S. Kleinbach, F. Meinert, F. Engel, W. J. Kwon, R. Löw, T. Pfau, and G. Raithel, Phys. Rev. Lett. **118**, 223001 (2017).
- [15] E. L. Hamilton, C. H. Greene, and H. R. Sadeghpour, J. Phys. B: At. Mol. Opt. Phys. **35**, L199 (2002).
- [16] M. I. Chibisov, A. A. Khuskivadze, and I. I. Fabrikant, J. Phys. B: At. Mol. Opt. Phys. **35**, L193 (2002).
- [17] V. Bendkowsky, B. Butscher, J. Nipper, J. P. Balewski, J. P. Shaffer, R. Löw, T. Pfau, W. Li, J. Stanojevic, T. Pohl, and J. M. Rost, Phys. Rev. Lett. **105**, 163201 (2010).
- [18] D. A. Anderson, S. A. Miller, and G. Raithel, Phys. Rev. A **90**, 062518 (2014).
- [19] F. Böttcher, A. Gaj, K. M. Westphal, M. Schlagmüller, K. S. Kleinbach, R. Löw, T. Cubel Liebisch, T. Pfau, and S. Hofferberth, Phys. Rev. A **93**, 032512 (2016).
- [20] J. L. MacLennan, Y.-J. Chen, and G. Raithel, Phys. Rev. A **99**, 033407 (2019).
- [21] M. T. Eiles and C. H. Greene, Phys. Rev. A **95**, 042515 (2017).
- [22] S. Markson, S. T. Rittenhouse, R. Schmidt, J. P. Shaffer, and H. R. Sadeghpour, Chem. Phys. Chem. **17**, 3683 (2016).
- [23] A. A. Khuskivadze, M. I. Chibisov, and I. I. Fabrikant, Phys. Rev. A **66**, 042709 (2002).
- [24] O. Thomas, C. Lippe, T. Eichert, and H. Ott, Nat. Commun. **9**, 2238 (2018).

- [25] W. Li, I. Mourachko, M. W. Noel, and T. F. Gallagher, Phys. Rev. A, **67**, 052502 (2003).
- [26] J. Han, Y. Jamil, D. V. L. Norum, P. J. Tanner, and T. F. Gallagher, Phys. Rev. A, **74**, 054502 (2006).
- [27] J. E. Sansonetti, Journal of Physical and Chemical Reference Data, **35**, 301 (2006).
- [28] E. Arimondo, M. Inguscio, and P. Violino, Rev. Mod. Phys. **49**, 31 (1977).
- [29] F. Hummel, C. Fey, and P. Schmelcher, Phys. Rev. A, **97**, 043422 (2017).
- [30] C. Bahrim and U. Thumm, Phys. Rev. A **61**, 022722 (2000).
- [31] S. Schmid, A. Härter, A. Frisch, S. Hoinka, and J. Hecker Denschlag, Rev. Sci. Instrum. **83**, 053108 (2012).
- [32] A. Härter, A. Krüchow, A. Brunner, and J. Hecker Denschlag, Appl. Phys. Lett. **102**, 221115 (2013).
- [33] J. Wolf, M. Deiß, A. Krüchow, E. Tiemann, B. P. Ruzic, Y. Wang, J. P. D’Incao, P. S. Julienne, and J. Hecker Denschlag, Science **358**, 921 (2017).
- [34] T. Niederprüm, O. Thomas, T. Manthey, T. M. Weber, and H. Ott, Phys. Rev. Lett. **115**, 013003 (2015).
- [35] M. Schlagmüller, T. C. Liebisch, F. Engel, K. S. Kleinbach, F. Böttcher, U. Hermann, K. M. Westphal, A. Gaj, R. Löw, S. Hofferberth, T. Pfau, J. Pérez-Ríos, and C. H. Greene, Phys. Rev. X **6**, 031020 (2016).
- [36] S. Bize, Y. Sortais, M. S. Santos, C. Mandache, A. Clairon, and C. Salomon, Europhys. Lett. **45**, 558 (1999).
- [37] The operator $\vec{\nabla}_{\vec{r}} \cdot \delta(\vec{R} - \vec{r}) \vec{\nabla}_{\vec{r}}$ is a shorthand for $\sum_{i,j} |\psi_i\rangle \langle \psi_j| \int d^3r \delta(\vec{R} - \vec{r}) \left(\vec{\nabla}_{\vec{r}} \psi_i^*(\vec{r}) \right) \cdot \left(\vec{\nabla}_{\vec{r}} \psi_j(\vec{r}) \right)$, where the $\{|\psi_i\rangle\}$ form an orthonormal basis of the Hilbert space and $\psi_i(\vec{r}) \equiv \langle \vec{r} | \psi_i \rangle$.
- [38] F. Hummel, C. Fey, and P. Schmelcher, Phys. Rev. A, **99**, 023401 (2019).
- [39] It has been predicted that $|\Omega\rangle$ -splittings due to $\vec{L} \cdot \vec{S}$ interaction should be observable without ambiguity in the case of S -state ultralong-range Rydberg molecules for which fine structure is negligible [38].
- [40] C. Fey, M. Kurz, P. Schmelcher, S. T. Rittenhouse, and H. R. Sadeghpour, New J. Phys. **17**, 055010 (2015).
- [41] E. P. Wigner, Phys. Rev., **98**, 145 (1955).
- [42] H. Köppel, W. Domcke, and L. S. Cederbaum, Adv. Chem. Phys. **57**, 59 (1984).
- [43] S. Haze, J. Wolf, M. Deiß, L. Wang, G. Raithel, and J. Hecker Denschlag, arXiv:1901.11069 (2019).
- [44] N. V. Ewald, T. Feldker, H. Hirzler, H. Fürst, and R. Gerritsma, arXiv:1809.03987 (2018).
- [45] F. Engel, T. Dieterle, T. Schmid, C. Tomschitz, C. Veit, N. Zuber, R. Löw, T. Pfau, and F. Meinert, Phys. Rev. Lett. **121**, 193401 (2018).